
Polarized X-rays Correlated with Short-Timescale Variability of Cygnus X–1 Letter

Kaito NINOYU^{1,*}, Yuusuke UCHIDA^{1,*}, Shinya YAMADA^{2,*}, Takayoshi KOHMURA¹, Taichi IGARASHI^{2,3}, Ryota HAYAKAWA^{2,4} and Tenyo KAWAMURA²

¹Department of Physics and Astronomy, Tokyo University of Science, 2641 Yamazaki, Noda, Chiba 278-8510, Japan

²Department of Physics, Rikkyo University, 3-34-1 Nishi Ikebukuro, Toshima-ku, Tokyo 171-8501, Japan

³Division of Science, National Astronomical Observatory of Japan, Tokyo, Japan

⁴International Center for Quantum-field Measurement Systems for Studies of the Universe and Particles (QUP), KEK, 1-1 Oho, Tsukuba, Ibaraki 305-0801, Japan

*E-mail: 6223525@ed.tus.ac.jp, yuuchida@rs.tus.ac.jp, syamada@rikkyo.ac.jp

Received ; Accepted

Abstract

We systematically investigate the variability of polarized X-rays on a timescale of a few seconds in the low/hard state of the black hole binary Cygnus X–1. The correlation between polarization degrees and angles with X-Ray intensity was analyzed using data collected by the Imaging X-ray Polarimetry Explorer (IXPE) in June 2022. Given that X-Ray variability in the low/hard state of Cygnus X–1 is non-periodic, flux peaks were aggregated to suppress statistical fluctuations. We divided the temporal profiles of these aggregated flux peaks into seven time segments and evaluated the polarization for each segment. The results reveal that the polarization degree was $4.6\% \pm 1.2$ and $5.3\% \pm 1.2$ before and after the peak, respectively, but decreased to $3.4\% \pm 1.1$ and $2.7\% \pm 1.1$ in the segments including and immediately following the peak. Furthermore, the polarization angle exhibited a slight shift from approximately 30° to $\sim 40^\circ$ before and after the peak. These findings suggest that the accretion disk contracts with increasing X-Ray luminosity, and the closer proximity of the X-Ray emitting gas to the black hole may lead to reduced polarization.

Key words: polarization — accretion, accretion disk — X-rays:binaries — X-rays:individual(Cyg X–1)

arXiv:2408.00980v1 [astro-ph.HE] 2 Aug 2024

1 Introduction

Cygnus X–1 (Cyg X–1) stands as one of the most celebrated black hole binary (BHB) systems. This system is composed of a black hole with a mass of 21.2 ± 2.2 solar masses and a companion blue giant star with a mass of $40.6^{+7.7}_{-7.1}$ solar masses, located at a distance of 2.2 kpc (Miller–Jones et al. 2021). The black hole accumulates material from its companion star, forming accretion flows that heat up to several million Kelvin. Cyg X–1 is known to display two distinctive spectral features (Done, Gierliński & Kubota 2007): the high/soft state and the low/hard state. In the high/soft state, radiation in the soft X–ray band is predominantly due to multi black-body radiation from the accretion disk (e.g., Tomsick et al. 2014; Walton et al. 2016). Conversely, in the low/hard state, radiation is dominated by inverse Compton scattering in the corona (e.g., Makishima et al. 2008; Yamada et al. 2013a), characterized by a high-temperature electron cloud with $kT_e \sim 100$ keV and their reflection components by the accretion disk including the fluorescence iron–K lines (Fabian et al. 2012). Spectral and timing analysis was used to investigate the structure and radiation mechanism of the accretion flows, in particular spectroscopy of the energy spectrum (e.g., Basak et al. 2017; Krawczynski & Beheshtipour 2022), the time lag of the X–ray variability between different energy bands (e.g, Nowak et al. 1999; Pottschmidt et al. 2000) or the power spectra showing X–ray variability in frequency space (e.g., Axelsson & Done 2018; Mahmoud & Done 2018). Determining the detailed geometries has been difficult due to modeling degeneracies, requiring alternative approaches.

The black hole accretion flow often emits X–rays with distinct polarization characteristics. Such X–ray polarization is believed to arise from multiple sources, including radiation from within the accretion disk (Schnittman & Krolik 2009), Compton scattering in the corona, radiation reflections off the accretion disk, and outflows (Poutanen, Nagendra & Svensson 1996; Schnittman & Krolik 2010). These polarized X–rays offer clues about the distribution of accretion flow close to the black hole and help elucidate the geometry of both the accretion disk and corona. The Eighth Orbiting Solar Observatory (OSO–8) detected the polarization of Cyg X–1 for the first time (Long, Chanan & Novick 1980; Weisskopf et al. 1977). After around forty years, PoGO+ observations revealed that the upper limit of polarization degree is 8.6% and the polarization angle is parallel to the jet axis in the high energy band of 19–181 keV (Chauvin et al. 2018). A remarkable observation of Cyg X–1 using the Imaging X–ray Polarimetry Explorer (IXPE; Weisskopf et al. 2022) in May 2022 revealed a po-

larization degree of $4.0 \pm 0.2\%$ and a polarization angle of $-20^\circ.7 \pm 1^\circ.4$ (Krawczynski et al. 2022, hereafter K22), which is higher than expectations of a polarization degree of $\sim 1\%$ (Krawczynski & Beheshtipour 2022). Notably, this is in alignment with the jet position angle (Stirling et al. 2001) observed in the 2–8 keV range. Such findings suggest a corona distributed perpendicular to the direction of the jet and in alignment with the accretion disk. Interestingly, even this geometry of accretion disk and corona struggles to account for the high polarization of 4% at a low inclination angle $27^\circ.1 \pm 0^\circ.8$ (Orosz et al. 2011), hinting at the need for a inclination angle exceeding 45° . As X–ray polarization offers a window into the dynamics around black holes, any rapid changes in the accretion flow’s structure could lead to accompanying shifts in polarization patterns.

Cyg X–1 has consistently exhibited intensity variability on short duration spanning a few seconds particularly in its the low/hard state, as documented by prior studies such as Miyamoto et al. (1992), Negoro et al. (1994, hereafter N94), and Yamada et al. (2013b, hereafter Y13). Given that each observed peak in the X–ray variability tends to be of relatively low amplitude and non-period, and thus lacks sufficient statistical robustness, there is an imperative to aggregate these peaks for improved clarity. N94 introduced the “shot analysis” and applied it to the observation of Cyg X–1 with Ginga, and Y13 applied it to the observation of Cyg X–1 with Suzaku. They were found to be time-symmetric in terms of the characteristics of the intensity change from brightening to darkening. The hardness ratio of the N94 and Y13 profiles up to 60 keV and 200 keV, respectively, shows that the profiles become softer toward the peak and harder rapidly after the peak. Y13 revealed the variability of the Compton component parameters (the electronic temperature, optical depth and y -parameter) with an intensity variation and suggested that they can be explained by physical phenomena in the accretion flow at ~ 1 s or less.

To investigate the short-timescale polarization variability, we focused on analyzing the rapid intensity variability. In this letter, we show that we have explored the properties of the polarization variability by polarization detection method with aggregation of X–ray intensity peaks.

2 Observation and Data Reduction

IXPE can acquire enough statistics to detect the rapid variability of the polarization, thanks to its high sensitivity of polarization detection. Carrying three detector units (DUs), each paired with a Mirror Module Assembly, the design of IXPE is optimal for the X–ray polarimeters. The Gas Pixel Detectors (GPDs) on board each DUs achieve

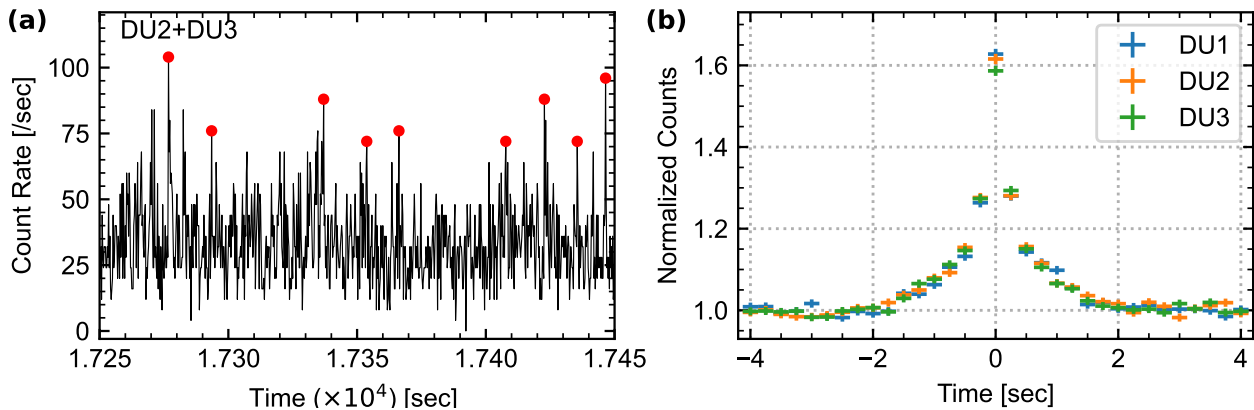


Fig. 1. Combined light curve and profile of aggregated X-ray peaks across detector units. (a), Light curve constructed from the combined data of DU2 and DU3. The x-axis indicates the elapsed time since the beginning of the observation, and the y-axis shows the count rate with a temporal resolution of 0.25 s. Detected peaks of X-ray flux are emphasized in red. (b), Separate profiles for each detector unit: DU1 in blue, DU2 in orange, and DU3 in green.

polarization for incident polarized X-ray photons in the energy band of 2–8 keV by measuring the electric field direction of each incident polarized X-ray photon, as detailed in Baldini et al. (2021). For a comprehensive understanding of the polarization measurement principle employed by GPD, readers are directed to Di Marco et al. (2022), Muleri (2022) and Baldini et al. (2022).

Cyg X–1 underwent observations via IXPE on six separate occasions between May 2022 and June 2024. For the purpose of this study, we focused on the low/hard state observations: specifically, the 246 ks observation from 15 May 2022 and the 81 ks observation from 12 June 2022. Our analysis involved the examination of Level–2 data, processed primary data collected by GPD through the instrumental pipeline, and we analyzed the data using `ixpeobssim` (Baldini et al. 2022), version 30.6.3. The extraction of source events was executed from a circular region with a radius of 150 arcsec centered on Cyg X–1, specifically in the 2–8 keV energy range, utilizing the `ixpeobssim/xpselect`. The observed region was notably luminous, rendering background effects negligible (Di Marco et al. 2023).

From the two observation in May and June of 2022, we measured the polarization degrees and angles of $3.99 \pm 0.20\%$, $-21^\circ.3 \pm 1^\circ.4$ and $3.8 \pm 0.3\%$, $-25^\circ.4 \pm 2^\circ.3$, respectively by `ixpeobssim/xpbin` PCUBE algorithm (Rankin et al. 2022; Kislat et al. 2015). These values are consistent with the previous study (K22). The two observations are consistent in terms of the polarization information. K22 mentioned the May observation highlighted energy dependence. On the other hand, for the June observation, we measured the polarization degree was not significantly changed with energy as $3.7 \pm 0.3\%$ at 2–4 keV, $4.0 \pm 0.5\%$ at 4–6 keV and $3.8 \pm 1.1\%$ at 6–8 keV. This disparity hints at variances in the origins of polarization, potentially tied

to differences in accretion flows during each observation. Consequently, we approached the analysis of these observations, spaced a month apart, as distinct episodes and show the results of the June 2022 observation.

3 Data Analysis and Results

3.1 Analysis of aggregated X-ray intensity peaks

We aggregated the peaks of the X-ray intensity obtained with IXPE light curve, referring to the previous shot analysis (N94; Y13). We created three light curves for each DU with a temporal bin size of 0.25 seconds, enabling the examination of variations below approximately 1 Hz. We first combined the light curves of two of the three DUs and used this combined light curve for the peak selection. Our criteria for peak selection involved assessing both the prominence and the inter-peak distances within the light curve. The prominence is the relative magnitude of the peaks and can efficiently eliminate small peaks. After testing various threshold settings, prominence showed to have a more critical influence on peak selection than inter-peak distance. We identified that a prominence of 60 counts/sec (corresponding to a 0.25-second bin) and an inter-peak distance of 8 s yielded the most statistically sound results and optimal polarization visibility (Figure 1(a)). At this step, this involves selectively identifying brighter peaks, including those misidentified due to Poisson noise. We therefore cross-referenced peak timings against the light curve from the uncombined DU, which was not utilized for peak selection process, and aggregated its photons. We identified 2546, 2825, and 2954 peaks for DU1, DU2, and DU3, respectively. Figure 1(b) displays the profile derived from these aggregated peaks and normalized using the average count rate observed from -4 s to -2 s and $+2$ s to $+4$ s

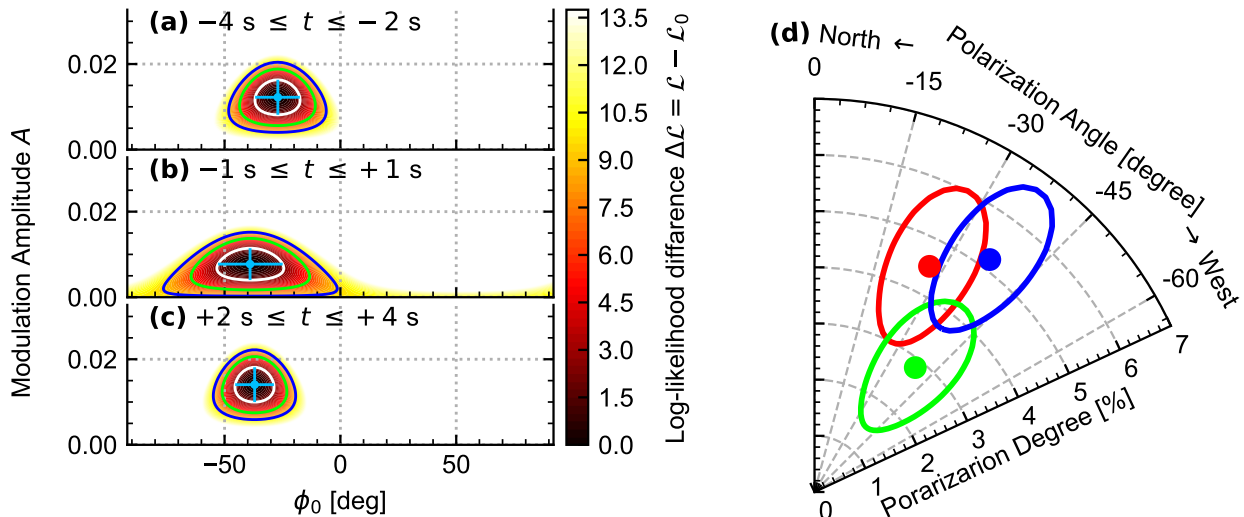


Fig. 2. Time-segment resolved polarization as deduced from the modulation curve. (a)–(c), Log-likelihood contours for parameters ϕ_0 and A across distinct time segments: (a) ($-4 \text{ s} \leq t \leq -2 \text{ s}$), (b) ($-1 \text{ s} \leq t \leq +1 \text{ s}$), and (c) ($+2 \text{ s} \leq t \leq +4 \text{ s}$). The confidence intervals are represented as 68.3% (white), 95.0% (green), and 99.0% (blue). Best-fit parameters are highlighted in cyan blue, with error bars signifying the 1σ (68.3% confidence level). Contour shows the distribution of differences of log-likelihood L from the minimum log-likelihood L_0 , the log-likelihood value at the estimated ϕ_0 and A . The minimum log-likelihood L_0 values for $-4 \text{ s} \leq t \leq -2 \text{ s}$, $-1 \text{ s} \leq t \leq +1 \text{ s}$, and $+2 \text{ s} \leq t \leq +4 \text{ s}$ intervals are 301.9, 305.2, and 290.0, respectively. (d) Polarization derived from assessed ϕ_0 and A values. Ellipses indicate the 68.3% confidence regions. Results for time segments are color-coded as: $-4 \text{ s} \leq t \leq -2 \text{ s}$, (red), $-1 \text{ s} \leq t \leq +1 \text{ s}$ (green), and $+2 \text{ s} \leq t \leq +4 \text{ s}$ (blue).

around the peak.

3.2 Time-segment resolved polarization

We partitioned the stacked profile into seven time segments and determined the polarization within each time segment to comprehensively study the polarization changes across distinct peak segment. Time segments were set to $\pm 1 \text{ s}$, centred on time points from -3 s to $+3 \text{ s}$ for 1 s each in the time relative to the peak time (time width of each segment was 2-second intervals). We identified events specific to each of these seven time segments from all three DUs and carried out polarization analysis.

For the determination of polarization, we employed three distinct methodologies. First, we utilized (1) `ixpeobssim/xpbin` PCUBE algorithm computational approach (Rankin et al. 2022; Kislat et al. 2015). Secondly, we conducted a (2) spectro-polarimetric fit using the `XSPEC` software (version v12.13.0c). Utilizing `XSPEC`, we simultaneously fitted the Stokes I , Q , and U spectra from all three DUs for every time segment. We used the constant polarization model `POLCONST` for polarization model in `XSPEC`. Cyg X-1 was in the hard state in this observation, so the chosen model was `CONST*TBABS*POLCONST*(DISKBB+NTHCOMP)`. Specific parameters were fixed: column density in `TBABS` at $4 \times 10^{21} \text{ cm}^{-2}$, norm in `DISKBB` at 4000 and kT_e in `NTHCOMP` at 100 keV, and kT_{bb} was linked to `DISKBB`. As these fixed

parameters are not determined by the IXPE band alone, we refer to K22, which reported the same hard state. The constant parameter is fixed to 1.0 at DU1, while those of the other two units are not fixed and determined as 0.9661 ± 0.0012 and 0.9197 ± 0.0011 , respectively. Lastly, we performed (3) a modulation curve evaluation based on binned likelihood fitting (for more detailed in Appendix). A precedent Hitomi Collaboration et al. (2018), showcased the viability of employing this curve to distill X-ray polarization insights in a case of limited statistics. It is prudent to ascertain the consistency between statistical outcomes using `ixpeobssim/xpbin` and `XSPEC` and inferences drawn from the modulation curve.

Figures 2(a)–(c) present the log-likelihood contours, derived from the likelihood estimation of the modulation curve’s polarization amplitude A and polarization angle ϕ_0 for each three distinct intervals: $-4 \text{ s} \leq t \leq -2 \text{ s}$, $-1 \text{ s} \leq t \leq +1 \text{ s}$, and $+2 \text{ s} \leq t \leq +4 \text{ s}$. The log-likelihood within the time segment $-1 \text{ s} \leq t \leq +1 \text{ s}$ confirms polarization detection at a 95.5% confidence level, whereas the other time segments record a robust 99.9%. The time segment around the intensity peak, despite the higher number of photons before and after the peak segment, suggests that the anisotropy of photoelectrons changes not in any particular direction, but yielding the reduction of the modulation amplitude. As shown in Figure 2(d), polarizations derived from the modulation amplitude A indicate that the polarization degree preceding and succeeding the maximum

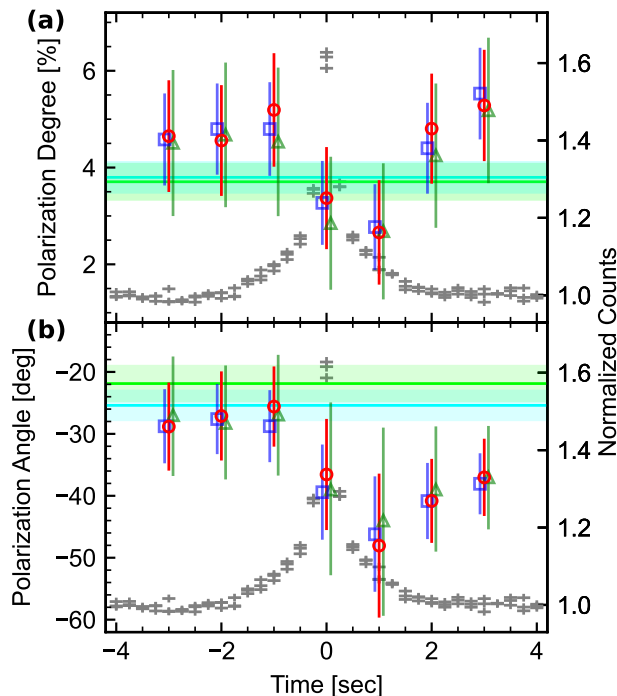


Fig. 3. Intensity-correlated variability of polarization on a short-timescale. (a), Polarization degree and (b), Polarization angle, determined through three different analytical methods. Error bars indicate a 68.3% confidence interval (1σ). Data are presented with a slight offset along the x-axis for visual clarity and are color-coded based on the analytical method used: `xpeobssim/xpbin` (red circle), `XSPEC` (blue squared), and modulation curve (green triangle). For visual clarity, the normalized counts of intensity variability are presented on the two figures with the right axis. As a reference, the polarization averaged over the entire observation and outside the time segment of $-4 \leq t \leq +4$ are shown in cyan and lime solid lines, where the patched regions indicate a 68.3% confidence interval.

of the profile of the stacked peaks stands at $4.6 \pm 1.2\%$ and $5.3 \pm 1.2\%$ respectively. Interestingly, the polarization degree reduces to $3.4 \pm 1.1\%$ at the peak (within a ± 1 second range). Concurrently, the polarization angles exhibit minor variability, hovering around $\sim 30^\circ$.

Figure 3 displays the polarization degrees and the polarization angles for all time segment among the shot duration, obtained through the three independent methods (summarized in Table 1). Our assessment of polarization approached via three distinct methodologies, yielded consistent outcomes. The polarization angle appears to be smaller than the time average. This is because the polarization angle is smaller in the extracted intensity variability, and the polarization angle outside the time segment of the intensity variability corresponds to the time average. When comparing segment $-2 \text{ s} \leq t < +0 \text{ s}$ and $+0 \text{ s} \leq t \leq +2 \text{ s}$ — characterized by non-overlapping computed intervals —, we discerned a shift in the polarization degree within a 1σ boundary. The polarization degree before the peak was $5.2 \pm 1.2\%$ and after the peak decreased

to $2.7 \pm 1.1\%$. The polarization angle also changed at the period immediately after the peak. While the statistical robustness of the findings is not yet optimal, the results suggest a potential temporal lag between polarization degree and intensity variability, where the polarization degree decreases on a timescale of seconds following the peak of the luminosity enhancement.

4 Discussion and Conclusion

The observed short-timescale correlation with spectral changes, advances our comprehension of the accretion dynamics proximate to the black holes. The observed correlation among increase in X-ray intensity, softening of the spectrum and decrease in polarization is be able to interpret the observed luminosity increase as the inner edge of the standard accretion disk approaching the black hole (also reported in (Bhargava et al. 2022)). The increase in unpolarized or low-polarized radiation due to the inner accretion disk edge being closer to the black hole may have softened the spectrum (the accretion disk component is at the lower energy side down to $\sim 3 \text{ keV}$) and reduced the total polarization (Table 1). Also, following the context of stronger radiation originating from the accretion disk from the vicinity of the black hole, there is a difference in polarization angle between the direct radiation from the accretion disk and the scattered radiation in the corona. Consequently, the mixing of two or more polarization angle directions has the effect of reducing the polarization degree. This phenomenon explains the change in polarization angle and the reduction in the modulation of the modulation curve as shown in Figure 2 and 3.

Intensity variability on the scale of a few seconds are related to mass accretion and can be compared with the structural changes associated with the transition from the low/hard to the high/soft state. Jana & Chang (2024) reported that they observed differences in the polarization of different hard and soft states of Cyg X-1. The authors suggested that the optical thickness of the corona in the soft state increased the scattering frequency of the seed photons and reduced the polarization. The decrease in polarization shown in this study can also be naturally explained by the density change due to the contraction of the corona near the black hole and the increase in the number of scattering of seed photons. Conventionally, regions with lower optical depth would exhibit less frequent scattering events, thus resulting in more pronounced polarization of Compton radiation (Poutanen, Veledina & Beloborodov 2023), a scenario that diverges from our empirical findings. Also, there is no valid explanation for the change in polarization angle.

Table 1. Polarization results (Polarization Degree (PD) and Polarization Angle (PA)) from three analysis methods and the best-fitting parameters across seven time segments. These results were derived using three distinct methods: `xpbin`, `XSPEC` and modulation curve.

Time Segment [s]	$-4 \leq t \leq -2$	$-3 \leq t \leq -1$	$-2 \leq t < 0$	$-1 \leq t \leq 1$	$0 \leq t \leq 2$	$1 \leq t \leq 3$	$2 \leq t \leq 4$
PD* [%]	4.6 ± 1.2	4.6 ± 1.1	5.2 ± 1.2	3.4 ± 1.1	2.7 ± 1.1	4.8 ± 1.1	5.3 ± 1.2
PD† [%]	4.6 ± 1.0	4.8 ± 1.0	4.8 ± 1.0	3.3 ± 0.9	2.8 ± 0.9	4.4 ± 1.0	5.5 ± 1.0
A/A_{100} [%]	4.5 ± 1.5	4.7 ± 1.5	4.5 ± 1.5	2.9 ± 1.4	2.7 ± 1.4	4.2 ± 1.5	5.2 ± 1.5
PA* [deg]	-29 ± 7	-27 ± 7	-26 ± 6	-37 ± 9	-48 ± 12	-40 ± 6	-37 ± 6
PA† [deg]	-29 ± 6	-28 ± 6	-29 ± 6	-39 ± 8	-46 ± 9	-41 ± 6	-38 ± 5
ϕ_0 [deg]	-27 ± 10	-28 ± 9	-26 ± 10	-39 ± 14	-44 ± 15	-39 ± 10	-37 ± 8
T_{in} [keV]	$0.352^{+0.016}_{-0.020}$	$0.350^{+0.017}_{-0.022}$	$0.353^{+0.018}_{-0.024}$	$0.387^{+0.012}_{-0.015}$	$0.382^{+0.012}_{-0.015}$	$0.359^{+0.015}_{-0.019}$	$0.365^{+0.014}_{-0.017}$
Gamma	$1.83^{+0.016}_{-0.017}$	$1.836^{+0.016}_{-0.017}$	$1.849^{+0.017}_{-0.018}$	$1.823^{+0.017}_{-0.018}$	$1.805^{+0.017}_{-0.018}$	$1.812^{+0.016}_{-0.017}$	$1.810^{+0.017}_{-0.018}$
$\chi^2/\text{d.o.f}$	1401/1336	1413/1336	1440/1336	1415/1336	1392/1336	1362/1336	1369/1336
F_{4-8}/F_{2-4} ‡	1.129 ± 0.005	1.127 ± 0.005	1.119 ± 0.005	1.119 ± 0.005	1.135 ± 0.005	1.141 ± 0.005	1.143 ± 0.005

* Analysis method: `ixpeobssim/xpbin`† Analysis method: `XSPEC`

‡ un-absorbed flux ratio

Additionally, other phenomena could be involved. For instance, it could be argued that the inflows and outflows in relatively short times affects the polarization (Poutanen, Veledina & Beloborodov 2023), or else that the strong gravitational field of the black hole bends the light rays and rotates polarization. Moreover, the time lag between variability in polarization degree and angle and increase in X-ray intensity may represent a complex accretion process in the black hole binary. At the very least, the variability of polarization information suggests that a dynamic change in the accretion flow near the black hole. However, to verify this phenomenon, it is essential to observe polarization with good time resolution and sufficient statistics and a more detailed study of broader bandwidth polarized X-ray observations.

For a deep understanding, it is desirable to investigate radiations across a wider polarization spectrum. By analyzing the rapid polarization variability in diverse astrophysical objects like black hole binaries, blazars, AGNs, and ultra-luminous sources, we can deepen our knowledge of the physics governing black holes. Furthermore, the technique of stacking analysis to detect polarization changes holds potential for broader application to other compact objects, such as accreting neutron stars or white dwarfs, exhibiting aperiodic intensity fluctuations.

Acknowledgments

This research used data products provided by the IXPE Team (MSFC, SSC, INAF and INFN) and distributed with additional software tools by the High-Energy Astrophysics Science Archive Research Center (HEASARC), at NASA Goddard Space Flight Center (GSFC). This work was supported by JSPS KAKENHI Grant Number JP22H01272, JP20K20527, 22H01269, 21K1394, and 23K22540.

Appendix 1 Polarization Estimation Procedure through Modulation Curve

The essence of polarization analysis lies in discerning the anisotropic distribution of photoelectron trajectories within the detector, called modulation curve. The GPDs of IXPE are designed to specialize in mapping this anisotropy, particularly through the azimuthal angle of photoelectron tracks during photoelectric absorption when the GPD detects polarized X-ray photons. Subsequently, polarization details are extracted by translating this anisotropy into the Stokes parameters, Q and U , customized for each recorded event.

To compute azimuthal angles of emitted photoelectrons for each event, designated as k for k -th event, we applied the equation:

$$u_k \sim \sin(2\phi_k), \quad q_k \sim \cos(2\phi_k). \quad (\text{A1})$$

Here, u_k , and q_k represents the Stokes parameters for individual event and ϕ_k represents the azimuthal angle in sky coordinates. The symbol denoting approximately equal is used due to the concentration of photons from luminous sources, such as Cyg X-1, around the center of the detector, where systematic errors are minimized, in contrast to the peripheries of the detectors (Rankin et al. 2022). We constructed a histogram by using the azimuthal angle ϕ_k , for every DU and subsequently aggregated the results from all units. To delineate the modulation curves and ascertain polarization properties, we employed a binned likelihood fit approach, according to methodologies presented in Hitomi Collaboration et al. (2018).

Subsequently, we conducted two distinct simulation observations using the `ixpeobssim/xpobssim`: one reflecting an unpolarized observation and the other illustrating

a 100% polarized observation. These simulations were based on the Cyg X–1 radiation parameters specific to each DU. We set the spectral model for the simulation as `tbabs×(diskbb+nthcomp)`. The parameters were determined by fitting the spectral data from each DU for the observation periods in June 2022, utilizing `XSPEC`. For our simulations, exposure times were designated as 10^4 s for the unpolarized scenario and 10^5 s for the completely polarized case.

The expected counts for each i -th histogram bin, denoted as $n_{\text{exp}}(\phi_i)$, is formulated as:

$$n_{\text{exp}}(\phi_i) = n_{\text{sim}}(\phi_i) \{1 + A \cos[2(\phi_i - \phi_0)]\}. \quad (\text{A2})$$

Here, A represents the modulation curve's amplitude, ϕ_0 is the polarization angle in sky coordinates. It is postulated that n_{obs} adheres to a Poisson distribution. The likelihood function is given by:

$$L(\phi_0, A) = \prod_i \text{Poisson}[n_{\text{obs}}(\phi_i)/n_{\text{exp}}(\phi_i)]. \quad (\text{A3})$$

And its logarithmic transformation can be described as:

$$\mathcal{L} = -2 \log L. \quad (\text{A4})$$

To optimize the model, the maximum likelihood estimates for ϕ_0 and A are derived by minimizing the aforementioned logarithmic likelihood function. Denoting the minimal value of this function as L_0 , the difference, $\Delta\mathcal{L} = \mathcal{L} - \mathcal{L}_0$, converges to a χ^2 -distribution. For the two free parameters, ϕ_0 and A , the $\Delta\mathcal{L}$ values of 2.30, 5.99, and 9.21 correspond to confidence levels of 68.3%, 95.0%, and 99.0%, respectively. We showed the $\Delta\mathcal{L}$ distribution in Figure 2(a).

The polarization degree Π was calculated using the following relation:

$$\Pi = \frac{A}{A_{100}} \quad (\text{A5})$$

Here, A_{100} signifies the amplitude of the modulation curve derived from a 100% polarized observation simulation. We evaluated the A_{100} value as 0.270 ± 0.001 for the observations conducted in June 2022. The evaluated results are shown in Figure 2(b). We identified events specific from all three DUs to each of seven time segments and subsequently amalgamated their modulation curves to produce a singular comprehensive curve. An assessment of the modulation curves for each time-segment was carried out, with polarization values estimated via a binned likelihood fit.

References

Axelsson, M., & Done, C., 2018, *MNRAS*, 480, 751-758
 Baldini, L., et al., 2021, *Astroparticle Physics*, 133, 102628
 Baldini, L., et al., 2022, *SoftwareX*, 19, 101194

Basak, R., Zdziarski, A. A., Parker, M., & Islam, N., 2017, *MNRAS*, 472, 4220-4232
 Bhargava, Y., Hazra, N., Rao, A. R., Misra, R., Bhattacharya, D., Roy, J., & Alam, M., 2022, *MNRAS*, 512, 6067-6077
 Chauvin, M., et al., 2018, *Nature Astronomy*, 2, 652-655
 Di Marco, A., et al., 2022, *AJ*, 164, 103
 Di Marco, A., et al., 2023, *AJ*, 165, 143
 Done, C., Gierliński, M., & Kubota, A., 2007, *A&AR*, 15, 1-66
 Fabian, A. C. et al., 2012, *MNRAS*, 424, 217-223
 Hitomi Collaboration, et al., 2018, *PASJ*, 70, 113
 Jana, A., & Chang, H., 2024, *MNRAS*, 527, 10837-10843
 Kislat, F., Clark, B., Beilicke, M., & Krawczynski, H., 2015, *Astroparticle Physics*, 68, 45-51
 Krawczynski, H., & Beheshtipour, B., 2022, *ApJ*, 934, 4
 Krawczynski et al., 2022, *Science*, 378, 650-654 (K22)
 Long, K. S., Chanan, G. A., & Novick, R., 1980, *ApJ*, 238, 710-716
 Mahmoud, R., & Done, C., 2018, *MNRAS*, 480, 4040-4059
 Makishima, K., et al., 2008, *PASJ*, 60, 585
 Miller-Jones, J. C. A., et al., 2021, *Science*, 371, 1046-1049
 Miyamoto, S., Kitamoto, S., Iga, S., Negoro, H. & Terada, K., 1992, *ApJL*, 391, L21
 Muleri, F., 2022, *Springer Nature Singapore*
 Negoro, H., Miyamoto, S. & Kitamoto, S., 1994, *ApJL*, 423, L127 (N94)
 Nowak, M. A., Vaughan, B. A., Wilms, J., Dove, J. B., & Begelman, M. C., 1999, *ApJ*, 510, 874-891
 Orosz, J. A., McClintock, J. E., Aufdenberg, J. P., Remillard, R. A., Reid, M. J., Narayan, R., & Gou, L., 2011, *ApJ*, 742, 84
 Pottschmidt, K., Wilms, J., Nowak, M. A., Heindl, W. A., Smith, D. M., & Staubert, R., 2000, *A&A*, 357, L17-L20
 Poutanen, J., Nagendra, K. N., & Svensson, Roland, 1996, *MNRAS*, 283, 892-904
 Poutanen, J., Veledina, A., & Beloborodov, A. M., 2023, *ApJL*, 949, L10
 Rankin, J., et al., 2022, *AJ*, 163, 39
 Schnittman, J. D. & Krolik, J. H., 2009, *ApJ*, 701, 1175-1187
 Schnittman, J. D. & Krolik, J. H., 2010, *ApJ*, 712, 908-924
 Stirling, A. M., Spencer, R. E., de la Force, C. J., Garrett, M. A., Fender, R. P. & Ogle, R. N., 2001, *MNRAS*, 327, 1273-1278
 Tomsick, J. A. et al., 2014, *ApJ*, 780, 78
 Walton, D. J. et al., 2016, *ApJ*, 826, 87
 Weisskopf, M. C., Silver, E. H., Kestenbaum, H. L., Long, K. S., Novick, R. & Wolff, R. S., 1977, *ApJL*, 215, L65-L68
 Weisskopf, M. C., et al., 2022, *J. Astron. Telesc. Instrum. Syst.*, 8, 026002
 Yamada, S., Negoro, H., Torii, S., Noda, H., Mineshige, S. & Makishima, K., 2013b, *ApJL*, 767, L34 (Y13)
 Yamada, S., Makishima, K., Done, C., Torii, S., Noda, H. & Sakurai, S., 2013a, *PASJ*, 65, 80